A Performance Analysis of a Parabolic Trough Collector Using Numerical Computation and Real-Time Parameters

Prashant Saini[1], Pradeep Kumar[1], Atul Dhar[1], Satvasheel Powar[1]

[1] Indian Institute of Technology Mandi, Mandi, (India)

Abstract

This study models the parabolic trough collector (PTC) to assess the efficiency and heat flux distribution at the cylindrical receiver tube's outer wall. The algorithm used is Monte Carlo Ray Tracing (MCRT). A few authors have published the equations and their methods for building the MCRT-based algorithm. This work shows a simple and straightforward technique for improving the accuracy of MCRT-based algorithms while reducing processing time. For the PTC receiver tube's outside wall, the MCRT heat flux is employed as an input for numerical computation. These computations are carried out using ANSYS (Fluent 18.1). Temperature-dependent features of the heat transfer fluid and thermal radiation between the glass wrap and the absorber tube are also considered. A solar steam plant was built by Protarget, Germany, and operated by LUIT Renewables India, and the experimental results of Sandia Laboratory in the USA are within 2% of the computational results. The effect of variations in the real-time parameters, such as solar radiation, heat transfer fluid mass flow rate, wind speed, and glass envelope effect on PTC efficiency, are investigated further. According to the findings of this study, the PTC efficiency is affected by all of these parameters.

Keywords: Monte Carlo Ray Tracing, Computational Fluid Dynamics, Heat Transfer Fluid, Effective Statistic Random Method, PTC, CSC, parallel computing.

1. Introduction

Due to the growing population worldwide, energy demand for technological and industrial growth is increasing rapidly. Fossil fuels play a significant role in furnishing such energy demand, leading to conventional resource depletion and contributing to global warming (Hang et al. (2008), Fan et al. (2017), Cheng et al. (2015)). According to the U. N. Sustainable Development Goal 9 (Industry, Innovation, and Infrastructure) report, India's industrial sector consumed 32 % of energy in 2014, 74 % of which was used for heating production only. Process heat requirements in the industry vary from 50 °C to 400 °C (Chargui et al. (2021), Bellos et al. (2020)). Solar energy is a powerful resource with the potential to meet this energy/heat requirement. Solar energy is abundant in nature and technologically suitable for commercial applications (Cheng et al. (2013), Vouros et al. (2020)). According to the 2019 International Energy Agency (IEA) report, gross world energy usage in 2017 was 1.6×10^{14} kWh. The World Energy Assessment report estimated that the total energy received from the Sun to the Earth's surface is approximately 1.4×10^{14} TWh. Using 1-2 % of received power can meet world energy requirements.

Solar photovoltaic modules convert solar energy directly to electricity. But they have significantly lower efficiency as compared to solar thermal (Bartela et al. (2021)). Different solar collectors are engaged for thermal use viz flat plate collectors, evacuated tube collectors, line-focus collectors, point-focus collectors, and concentration collectors (Tzivanidis et al. (2015), Saini et al. (2018)). The option of a solar thermal collector depends on heat (outlet temperature) requirements. CSCs can achieve high temperatures ranging from 100 °C to 500 °C compared to non-concentrating solar collectors. Solar concentrators focus on the receiver using lenses or mirrors. These lenses help focus solar radiation from relatively large areas onto a (smaller area) receiver, where radiation is (usually) used to generate steam (Khandelwal et al. (2019), Wang et al. (2014)). These temperature levels can easily meet industry requirements without increasing the atmospheric carbon footprint. Many studies reported using CSCs (Concentrating Solar Collectors) and mainly focusing on solar collectors converting lower-density solar energy to mechanical energy (Cheng et al. (2014), Almanza et al. (2002), Powar et al. (2020)). When run in a temperature range of 250 °C – 565 °C, the real-world devices assert the CSCs' energy conversion efficiency between 23 % and 35 %.

Many researchers investigated the collector's optical efficiency. Burkhard et al. (1973) deduced an empirical relationship to determine solar energy flux on an absorber surface. Using this analytical relationship, Burkhard et al. (1973) assess the tube's heat flux. Evans et al. (1977) established an integral relationship governing solar energy flux distribution over parabolic trough collector (PTC) flat absorbers. The surface slope error has been investigated and reflects the effect of slope error on severity (Tyagi et al. (2007)). Jeter et al. (1986) built an

Selection and/or peer review under responsibility of Scientific Committee
doi:10.18086/eurosun.2022.12.14 Available at http://proceedings.ises.org

integrated model for determining the distribution of solar energy on both types of absorber tubes, i.e., circular absorber tube and flat absorber tube. This resulting formulation helps to decide PTC's performance. Later, Jeter et al. (1986) developed a model that considered the non-uniform source and incorporated reflection, absorption, and transmission effects to determine the PTC's optical efficiency (Jeter et al. (1987)).
Since PTC efficiency is also controlled by several other factors, including solar radiation, heat transfer fluid's mass flow rate, heat transfer fluid temperature, and wind velocity, understanding the effect of these factors on PTC efficiency is required. To the best of our knowledge, no such study analyses these crucial parameters' effect on PTC conversion efficiency.
Complex mathematical equations are included in these model types (Wang et al. (2021)). Adjusting geometric and optical characteristics in these models, on the other hand, is inconvenient (Kalogirou 2012). Considering such issues, a straightforward and flexible approach is crucial for analyzing CSCs' optical performance for the various geometric conditions (Kulahli et al. (2019), Mechanics and Arbor, 1982). MCRT is one of the reliable tools to overcome these challenges (He et al. (2011)). It's a very flexible, convenient, and efficient tool for estimating and analyzing CSC's optical performance (Liang et al. (2017), Fan et al. (2018)). This article explains a simple and straightforward technique for developing an MCRT-based method to estimate solar flux distribution over the PTC receiver tube in a circumferential and axial orientation with greater accuracy. The output of the created MCRT model is coupled as one of the boundary conditions in Fluent 18.1 to predict the PTC solar flux distribution to evaluate PTC performance and heat transfer characteristics. PTC efficiency and effectiveness were investigated using numerical models for various real-time parameters (e.g., solar radiation, HTF mass flow rate, heat transfer fluid inlet temperature (HTF), and wind velocity). The effect of the glass envelope on PTC output in the absorber tube was also investigated. A new MCRT-based algorithm is developed and reported here to calculate the non-uniform heat flux on the receiver tube of PTC's outer wall, as explained in section 2. Using this algorithm, two cases (with and without a glass envelope) are simulated under different real-time parameters to determine the efficiency of PTC, as explained in section 3.

2. Model Description

This investigation has been done to determine the effect of real-time parameters that significantly impact the efficiency of PTC, including solar radiation, the mass flow rate of heat transfer fluid, the temperature of heat transfer fluid, and wind speed. An in-house MCRT code was developed to find out the heat flux on PTC. This heat flux was used as a boundary condition in Fluent for estimating the heat gain by the PTC.

2.1 Governing equations

In the presented case, the fluid flow is in a steady and turbulent state; the following governing equations have been used in the FLUENT 18.1 simulation (A. Inc. 2018, "ANSYS Fluent Theory Guide v18.1," ANSYS 18.1 Doc., vol. 15317, no. April, p. 850).
Mass conservation is represented by the continuity equation (1):

$$\frac{\partial}{\partial x_i}(\rho u_i) = 0 \qquad \text{(eq. 1)}$$

The momentum conservation integral equation is represented by equation (2):

$$\frac{\partial}{\partial x_i}\left(\rho u_i u_j\right) = -\frac{\partial p}{\partial x_i} + \frac{\partial}{\partial x_j}\left[(\mu_t + \mu)\left(\frac{\partial u_j}{\partial x_i} + \frac{\partial u_i}{\partial x_j}\right) - \frac{2}{3}(\mu_t + \mu)\frac{\partial u_l}{\partial x_l}\delta_{ij}\right] + \rho g_i \qquad \text{(eq. 2)}$$

The Reynolds analogy concept was used in turbulent momentum transfer for numerical modeling of turbulent heat transport. The modeled energy equation is represented by equation (3):

$$\frac{\partial}{\partial x_i}(\rho u_i T) = \frac{\partial}{\partial x_i}\left[\left(\frac{\mu}{Pr} + \frac{\mu}{\sigma_T}\right)\frac{\partial T}{\partial x_i}\right] + S_R + S_h \qquad \text{(eq. 3)}$$

Turbulent kinetic energy (k) is represented by equation (4), and the rate of dissipation of kinetic energy (ε) is represented by equation (5).

$$\frac{\partial}{\partial t}(\rho k) + \frac{\partial}{\partial t}(\rho k u_i) = \frac{\partial}{\partial t}\left[\left(\mu + \frac{\mu_t}{\sigma_k}\right)\frac{\partial k}{\partial x_j}\right] + G_k + G_b - \rho\varepsilon - Y_M + S_k \qquad \text{(eq. 4)}$$

ε-equation:

$$\frac{\partial}{\partial t}(\rho\varepsilon) + \frac{\partial}{\partial x_i}(\rho\varepsilon u_i) = \frac{\partial}{\partial x_j}\left[\left(\mu + \frac{\mu_t}{\sigma_\varepsilon}\right)\frac{\partial \varepsilon}{\partial x_j}\right] + C_1\frac{\varepsilon}{k}(G_k + C_{3\varepsilon}G_b) - C_{2\varepsilon}\rho\frac{\varepsilon^2}{k} + S_\varepsilon \qquad \text{(eq. 5)}$$

S_k and S_ε are user-defined source terms. k-ε model is a semi-empirical model based upon the model transport

equation to determine the turbulent kinetic energy (k) and turbulent kinetic energy dissipation rate (ε) when the flow is fully turbulent. μ_t is turbulent viscosity, and the generation of k, G_k is represented by

$$\mu_t = C_\mu \rho \frac{k^2}{\varepsilon} \; and \; G_k = \mu_t \frac{\partial u_i}{\partial x_j}\left(\frac{\partial u_i}{\partial x_j} + \frac{\partial u_j}{\partial x_i}\right)$$

The values of the standard constants are as follows:
$C_{2\varepsilon} = 1.92$, $\sigma_\varepsilon = 1.3$, $C_\mu = 0.09$, $C_{1\varepsilon} = 1.44$, $\sigma_k = 1.0$

2.2 Integration of FLUENT and MCRT method

The distribution of circumferential solar flux on the receiver tube of PTC was estimated by MCRT (Monte Carlo Ray Tracing) in-house developed code. The estimated distribution of solar energy flux was used in FLUENT 18.1 software as the boundary condition. In the MCRT code, a data file of heat flux is generated, and the FLUENT software processes this heat flux data file as one of the boundary conditions. The governing equations used in the FLUENT are discretized by using a finite volume method. The energy equation, along with the momentum equation, is discretized by the second upwind scheme. The thermal radiation between the glass envelope and receiver tube is considered by using an additional source term method as represented by the term S_h in the energy equation (equation 3). Natural convection due to the temperature-dependent properties of heat transfer fluid (Syltherm-800) is included in the momentum equation by including the density as a function of temperature. And gravity is putting on in the Fluent.

2.3 Monte-Carlo-based Ray Tracing

The MCRT code was written in C to estimate the solar radiation distribution on the receiver tube's outer wall. The effective statistical random method was used to calculate solar flux distribution over the receiver tube, as described in the literature (Ehrlich 2002, Hoff and Janni 1989).

In the next step, the Monte Carlo method defined a virtual ray tracing plane above the PTC. The distance between this plane and the device was randomly chosen (i.e., 5m) (Fig.1), as it does not affect the solar flux calculation. Each random ray from this virtual plane is perpendicular to the absorber tube and parabolic reflector. A random generation process defines the source point on the virtual plane. The Monte Carlo method is a computational algorithm that performs repeated random sampling to obtain numerical results. The Monte Carlo method is based upon the concept of randomness to solve numerical problems.

There are five ways to define PTC geometry, and two independent geometric parameters can program the PTC.

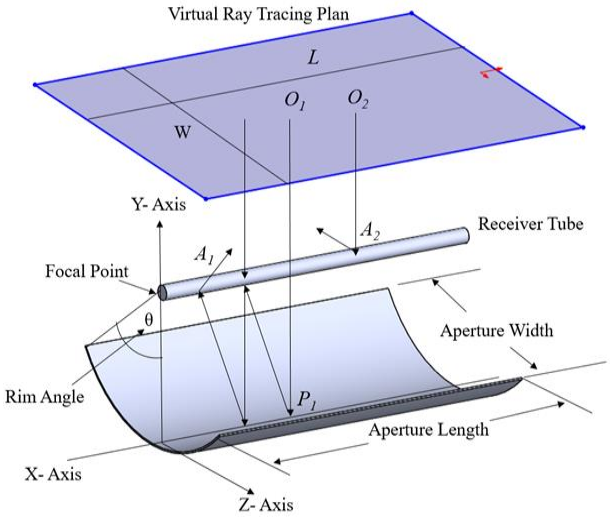

Fig. 1: Ray tracing virtual plan scheme

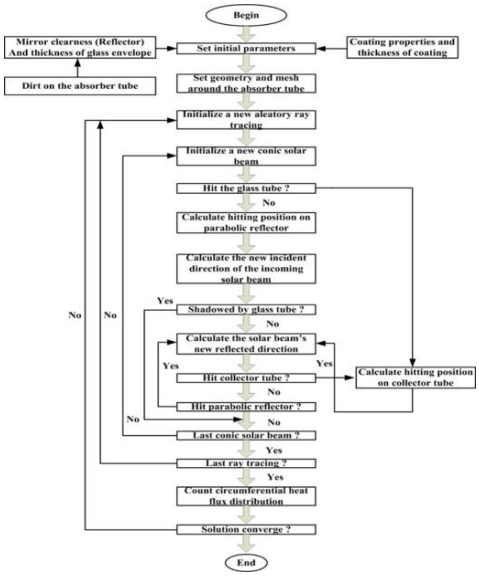

Fig. 2: Flow diagram of MCRT

The following methods can describe analytically deduced equations of PTC:

1. By specifying the focal point (f) and the parabola's aperture width (w), the rim angle (θ) is obtained. The parabola's coefficient (c) is related to focal length by equation (6).

c = 1/4f, and θ = 90° if b = 0, θ = arctan (0.5w/b) if b > 0, θ = 90° +arctan (b/0.5w) if b < 0 (eq. 6)

where b is the focal point distance.

2. By specifying the parabola's coefficient (c) and the aperture width (w), the parabola's focal point (f) is obtained by equation (7).

f = 1/4c and θ = 90° if b = 0, θ = arctan (0.5w/b) if b > 0, θ = 90° +arctan (b/0.5w) if b < 0 (eq. 7)

3. By giving the focal point *(f)* and the rim angle *(θ)*, the parabola's coefficient *(c)* is obtained from equation (6). The aperture width *(w)* is obtained by using equation (8).

$$w = \frac{-1+\sqrt{1+tan^2(\theta)}}{c*tan\,(\theta)}, if\ \theta < 90°, w = \frac{-1}{c}, if\ \theta = 90°, w = \frac{tan^2(\theta)+\sqrt{1+tan^2(\theta)}}{c}, if\ if\ \theta > 90° \quad \text{(eq. 8)}$$

4. With the specified parabola's coefficient *(c)* and the rim angle *(θ)*, the focal point *(f)* is calculated by using equation (7), and the aperture width *(w)* is obtained exactly the same as in case 3, by using equation (8).
5. With aperture width *(w)* and specified rim angle *(θ),* the focal point *(f)* is calculated by using equation (9).

$$f = \frac{w[1+\sqrt{1+tan^2(\theta)}]}{4tan\,(\theta)}, if\ \theta < 90°, f = \frac{w}{4}, if\ \theta = 90°, f = \frac{w[-tan\,(\theta)\ +\sqrt{1+tan^2(\theta)}]}{4tan\,(\theta)}, if\ if\ \theta > 90° \quad \text{(eq. 9)}$$

The total area of the absorber surface (A_a) and the estimated concentration factor are computed by using the equations (10-12).

$A_a = 2\,\pi\,R\,L$ (eq. 10)

Parabolic Reflector Surface Area (A_p) is estimated by equation (11).

$$A_p = \left[\frac{w}{2}t + \frac{1}{4c}\,ln\,ln\,(2c*w+t)\right]L \quad \text{(eq. 11)}$$

The concentrating factor (c_{fact},) relates the aperture width with the absorber's external radius, as shown by equation (12).

$$c_{fact} = \frac{w}{2\pi R} \quad \text{(eq. 12)}$$

In these equations: *R*: External radius of the absorber tube, *L*: Absorber tube length, *t* is obtained by the following equation: $t = \sqrt{(1+4w^2c^2)}$

For determining the total solar energy flux incidence on the absorber tube, an iterative process was performed. Each iterative loop generated a sequence of 1.8×10^8 rays tracing with starting points O_1, O_2, etc. (Fig. 1) located in the virtual ray tracing plane. Each ray tracing hits the system at different locations for the absorber tube (A_1) and the parabolic screen at points P_1. These hitting points are calculated by using the equations (13).

$x_i = x_i^o + t\cos(\alpha_i)$, where $i = 1,2,3\ldots\ldots$, (eq. 13)

where x_i^o are the coordinates of the source points located at the virtual ray tracing plane. Cos (α_i) is the ray tracing's direction cosines (0, -1, 0), and *(t)* is a parameter related to the linear vector function.

The parameter *(t)* is computed by the analytic solution of the quadratic equation (14).

The parameter *(t)* corresponds to the minimum value between the two roots t_1 and t_2 of equation (14).

$$t = \frac{-b \pm \sqrt{b^2-4ad}}{2a}, t = \min(t_1, t_2) \quad \text{(eq. 14)}$$

The normal external vector is built at the intersection point that was previously found by equation (13).

For the parabolic screen

$$n_x = 0;\ n_y = \frac{1}{\sqrt{1+4c^2x_3^2}}, n_z = \frac{-2cx_3^2}{\sqrt{1+4c^2x_3^2}} \quad \text{(eq. 15)}$$

For the absorber tube

$n_x = 0;\ n_y = cos(\theta_c);\ n_z = sin\,(\theta_c\,)$ (eq. 16)

Equation (18) represents the direction of the solar radiation on the PTC. The mean of the intersection points determines the angle (θ_c), where θ_c is the azimuthal angle at the absorber tube.

The unit reflected vector s^r is represented by equation (17) in vector and indicial notation.

$s^r = 2|s\cdot n|n - s,\ s_t^r = 2|s_j\cdot n_j|n_j - s_j,$ (eq. 17)

For determining the portion of the surface over the receiver tube, over which the solar radiation heat flux is added, a sequential search by discrete elements was developed. Each of the discrete elements on the absorber tube is divided into triangular elements.

The intersection points ***I*** within the triangular element is computed by using the equation (18).

$I_i = x_{si}^o + t_p\cos(\alpha_i)$ (eq. 18)

For three-node elements, the parameter *(t_p)* defines the intersection ***(I)*** between the solar beam and the triangular plane. The equation (19) is used for the computation of intersection point *(I)* within the triangular elements.

$$t_p = \frac{d - a_k x_{sk}^o}{a_k \cos(\alpha_k)} \quad \text{(eq. 19)}$$

Where a_k is the plane's coefficients defined by three points, and d is an independent term in equation (19).
If the intersection point belongs to the three nodes elements, the following condition represented by equation (20-21) must be satisfied for each component:

$$I_i = \beta_k x_i{}^k \text{ and } \sum_{k=1}^{3} \beta_k = 1 \quad \text{(eq. 20)}$$

The three values of coefficients (β_k) are obtained by the solution of the expression in equation (20), which produces a set of simultaneous equations (21).

$$\begin{matrix} x_1 & x_2 & x_3 \\ y_1 & y_2 & y_3 \\ z_1 & z_2 & z_3 \end{matrix} \times \begin{matrix} \beta_1 \\ \beta_2 \\ \beta_3 \end{matrix} = \begin{matrix} I_x \\ I_y \\ I_z \end{matrix} \quad \text{(eq. 21)}$$

The solution for each coefficient in equation (21) is given by equation (22).

$$\beta_k = \frac{I_k(y_l z_m - y_m z_l) + I_y(x_m z_l - x_l z_m) + I_z(x_l y_m - x_m y_l)}{\Delta} \quad \text{(eq. 22)}$$

Where sub-indices: *k*, *l*, and *m* follow a cyclic counter-clockwise permutation: *1-2-3*, and Δ is the matrix determinant.
If equation (21) is satisfied, then the solar energy flux is computed and added to the surface discrete elements. The local radiation energy in the unit area is computed by applying the numerical equation (23) for every ray tracing impacting on a specific discrete element around the absorber tube (Ehrlich 2002).

$$\dot{q}_r^e = \rho_{cl}\gamma a_e K(\theta_i)\psi(\theta_i) I_{bn} \text{ and } \rho_{cl} = 0.935, a_e = 0.023, \psi(\theta_i) = 1 \quad \text{(eq. 23)}$$

The user specifies the solar irradiance, I_{bn}. According to Kerlin et al. (2016), a default value of *1360.8 W/m²* was set in. The value of the intercept factor *(γ = 0.84)* was obtained from equation (24) (Padilla et al. (2011)).

$$\gamma = \prod_{i=1}^{6} \gamma_i \quad \text{(eq. 24)}$$

Where γ_1 = 0.950 (black chrome), γ_2 = 0.980 (collector mirror's geometrical accuracy), γ_3 = 0.960 (mirror clearness), γ_4 = 0.980 (dirt on heat collection element, i.e., absorber tube).
The incident angle modifier function $K(\theta_i)$ is defined by equation (25) (Gorantla et al. (2017)).

$$K(\theta_i) = cos(\theta_i) + 0.000884(\theta_i) - 0.00005369(\theta_i^2) \quad \text{(eq. 25)}$$

At the end of one cycle, when the 1.8×10^8 rays hit all the elements around the absorber tube, the total solar energy flux per unit area is computed by each element according to the Monte Carlo method by equation (26).

$$\dot{q}_e^L = \left(\frac{A_a}{A_e}\right)\left[\left(\frac{1}{N_a}\right)\sum_{r=1}^{N_r^e} q_r^e\right]_L \quad \text{(eq. 26)}$$

The total solar flux per unit area collected by the absorber tube is computed at the end of one cycle with the help of equation (27).

$$\dot{q}_e^L = \sum_{r=1}^{N_r^e} q_r^e \quad \text{(eq. 27)}$$

The relative error in the cycle of 1.8×10^8 rays is computed by using the equation (28).

$$Loop_{error} = \frac{|(\dot{q}_a^L)_{new} - (\dot{q}_a^L)_{old}|}{(\dot{q}_a^L)_{new}} \quad \text{(eq. 28)}$$

If the relative error is less than 0.0001, the convergence is attained, and the computation is finished; otherwise, another cycle of 1.8×10^8 rays tracings is performed until convergence is attained. Figure 2 represents the in-house developed algorithm's flowchart to calculate the heat flux on the receiver tube's outer surface using parallel computing. SEGS LS2 parabolic trough absorber tube was used to validate with the experimental comparison of Z. D. Cheng et al. (2010), as explained in section 2.7.

2.4 Boundary conditions

At the outlet of the PTC, a fully developed flow condition was applied. At the inlet of the absorber tube of PTC, a velocity magnitude of 1 m/s and HTF temperature of 303 K was applied. Other surfaces of the absorber tube of PTC were considered as adiabatic walls. At the absorber tube's outer cylindrical surface, circumferential heat flux calculated by the in-house developed MCRT method was applied. Syltherm-800 liquid oil was used as heat transfer fluid, and its properties are specified in Table 1. To couple the velocity and pressure, a SIMPLE algorithm is used. SIMPLE is used for solving pressure equations by using a semi-implicit method for compressible and incompressible fluid flow. In the SIMPLE algorithm, a second-order upwind scheme is used. The Nusselt number and Reynold number are calculated using the relation in Incropera and DeWitt (1990). A

computation domain five times larger than the PTC geometry was used to determine the effect of air. HTF with variable temperature is used to assess the impact of wind speed on the efficiency of PTC.

Tab. 1: Thermophysical properties of Syltherm-800

Temp (°C)	Specific heat (Kj/kg K)	Density (kg/m^3)	Thermal conductivity (W/m K)	Viscosity (mPa s)	Vapour pressure (kPa)
30	1.625	934.99	0.1331	8.32	0
80	1.711	881.68	0.1237	3.86	1.46
130	1.796	837.46	0.1143	2.11	13.5
180	1.882	792.08	0.1049	1.26	59.5
230	1.967	744.3	0.0955	0.81	171.7
280	2.052	692.87	0.0861	0.54	380.2

2.5 Grid independence study

Uniform structured mesh is used across the geometry, as shown in Figure 3. A grid independence study was conducted for PTC's absorber tube to predict performance and heat transfer characteristics. The minimum number of elements with grid-independent accuracy was 0.7 million; below that level, numerical calculation accuracy and solution stability changed with grid size, as seen in Figure 4. The element size implemented in the investigated case in this study was 0.005 × 0.005 m, with 0.7 million elements. Substantial computational effort and time were observed beyond 3.9 million elements corresponding to a grid size of 0.0025 × 0.0025 m. The volume mesh used has hexahedral-shaped elements. Figure 4 shows the curves of axial temperature variation at three circumferential locations corresponding to 0.7 million, 1.1 million, and 3.9 million elements, which are almost coinciding with each other. The figure shows that all respective curves are very close to each other, and the results show that the simulation model used is independent of grid size. To verify the grid independence of the solution, the model was run at three element sizes: 0.005 × 0.005 m, 0.0040 × 0.0040 m, and 0.0025 × 0.0025 m. These element sizes resulted in 0.7 million, 1.1 million, and 3.9 million elements in the geometry. Based on the finding of this study, a 0.7 million element count was used in all the simulations.

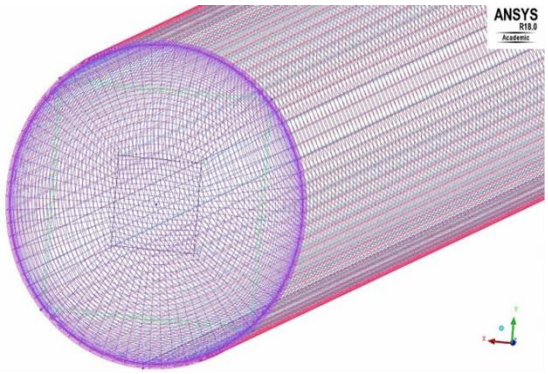

Fig. 3: Structured Mesh on the receiver tube of parabolic trough collector

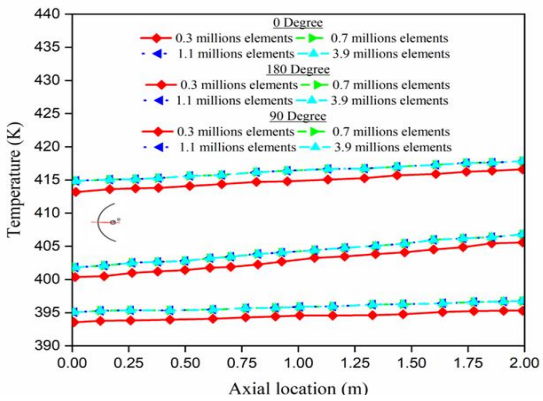

Fig. 4: Axial temperature on the receiver tube of the parabolic trough collector computed at four grid sizes (0.005 × 0.005 m, 0.0040 × 0.0040 m, 0.0025 × 0.0025 m and 0.0059 × 0.0059 m)

2.6 Experimental setup

Figure 5 (a) represents the schematic diagram of the PTC solar steam plant in Hatsun Agro Products in Salem (Tamil Nadu), India. This PTC solar steam plant has 2-rows of PTC and can be operated individually depending upon the need. This PTC solar steam plant has a minimum capacity of 900 kg of steam per day under temperature and pressure of 220 °C and 17.5 bar. The maximum capacity of this plant is 3 tonnes per day, and the average production of steam in this plant is 1.5 tonnes per day. Silicon-based heat transfer fluid is used in this system. The maximum thermal efficiency obtained in this system is 60%-65%. Figure 5 (b) depicts Hatsun Agro Products' actual PTC solar steam plant in Salem, Tamil Nadu (India).

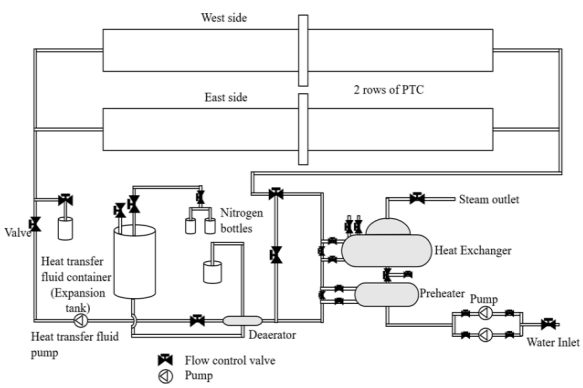

(a)

(b)

Fig. 5: (a) Schematic diagram of parabolic trough collector solar steam plant in Hatsun Agro Products, Salem (Tamil Nadu), India, and (b) Parabolic trough collector solar steam plant in Hatsun Agro Products, Salem (Tamil Nadu), India

2.7 Validation

Figure 6 shows that solar flux distribution in the circumferential direction over the PTC receiver tube using the MCRT method is in good agreement with the experimental results of Z. D. Cheng et al. (2010). Table 2 displays PTC dimensions for validation analysis, similar to the SEGS LS2 parabolic trough collector module tested on AZTRAK rotating platform at SNL by Dudley et al. (1994).

Tab. 2: Dimensions of the SEGS LS2 parabolic trough collector

S. No.	Parameters	Values
1.	Length of parabolic reflector (m)	7.8
2.	Width of parabolic reflector (m)	5
3.	Focal point (m)	1.84
4.	Outer diameter of receiver tube (mm)	70
5.	Outer diameter of a glass tube (mm)	115
6.	Inner diameter of receiver tube (mm)	66

Tab. 3: Experimental data and comparison with Z.D Chang et al. (2010) results with simulation results

Cases	I_r (W/m^2)	q_m (kg/s)	T_a (°C)	T_{in} (°C)	$T_{o,exp}$ (°C)	T_o (Z. D. Cheng.) (°C)	T_o	η (Exp.) (%)	η (Z. D. Cheng) (%)	η (%)
Case1	933.7	0.6782	21.2	102.2	124.0	126.8	126.09	72.51	72.64	72.47
Case 2	937.9	0.6206	28.8	297.8	316.9	319.4	316.36	67.98	68.35	68.20
Case 3	920.9	0.5457	29.5	379.5	398.0	401.9	398.53	62.34	62.69	62.40

Tab. 4: Experimental data of parabolic trough collector solar steam plant of "Hatsun Agro Products", Salem, Tamil Nadu (India) developed by Protarget, Germany & managed by LUIT Renewables and comparison of experimental results with simulation results

Cases	I_r (W/m^2)	q_m (kg/s)	T_a (°C)	T_{in} (°C)	$T_{o,exp}$ (°C)	T_o	η (Exp.) (%)	η (%)
Case1	794.90	0.7126	34	184.2	216.9	217.8	66.74	66.57
Case 2	848.78	0.6502	37	192.1	214.1	213.60	65.25	64.80
Case 3	810.71	0.5746	36	201.5	220.5	221.5	62.41	63.40

The energy absorption efficiency of the tube was calculated by using the equation (32).

$$\eta = k[73.3 - 0.007276\Delta T_{aa}] - 0.496(\Delta T_{aa}/I) - 0.0691(\Delta T_{aa}^2/I)$$

The new model on the MCRT method is also validated by comparing the efficiency results of Z.D. Chang et al. (2010) with the current study for the three different cases. The model was further validated by experimental data obtained from the PTC solar steam plant of Hatsun Agro Products in Salem, Tamil Nadu (India),

developed by Protarget, Germany, in collaboration with LUIT Renewables. Comparisons show close agreement with experimental data in Table 3 and Table 4. The maximum difference between the computed results of this study and the experimental data is less than 2%. This confirms the reliability of the new algorithm for the analysis of PTC absorber tubes.

3. Results and discussions

The variations in real-world parameters, including solar radiation, the inlet temperature of HTF, the mass flow rate of HTF, and wind speed on the efficiency of PTC, are analyzed and presented. The geometrical details of the PTC used for the numerical simulation are displayed in Table 5. Efficiency results are presented with and without a glass envelope over PTC's absorber tube. Subsequently, adding a glass envelope increases PTC's overall performance. As it prevents surrounding convective heat losses.

3.1 Solar radiation and distribution on receiver tube

Figure 7 (a) shows the solar flux distribution circumferentially over the receiver tube for the different solar radiations. For the different solar radiations, we have different solar flux. Here, solar flux on the receiver tube is directly proportional to solar radiation. Whereas, Figure 7 (b) shows the temperature on the outer wall of the receiver tube in the axial direction for the different values of θ (i.e., θ = 0°, 90°, 180°). This rise in the temperature in the axial direction can be observed in Figure 7 (b). The temperature is highest at θ = 90° as compared to θ = 0°, 180°. This is due to the reason that θ = 90° is on the side which has higher concentrated solar radiation while θ = 0° is on that side which has the lowest solar concentration. And θ = 180° on the side, which lies in between the concentrated solar region. The trends for the temperature and the circumferential solar distribution is quite similar to that of Z. D. Cheng et al. (2010).

Tab. 5: The dimensions of the parabolic trough collector

S. No.	Parameters	Values
1.	Length of the parabolic reflector (m)	2
2.	Focal point (mm)	220
3.	Width of parabolic reflector (m)	1
4.	Outer diameter of absorber tube (mm)	32

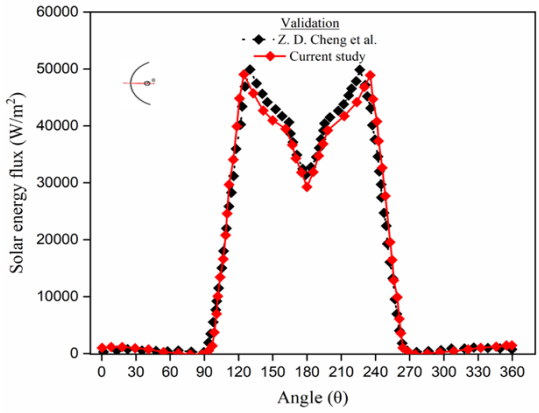

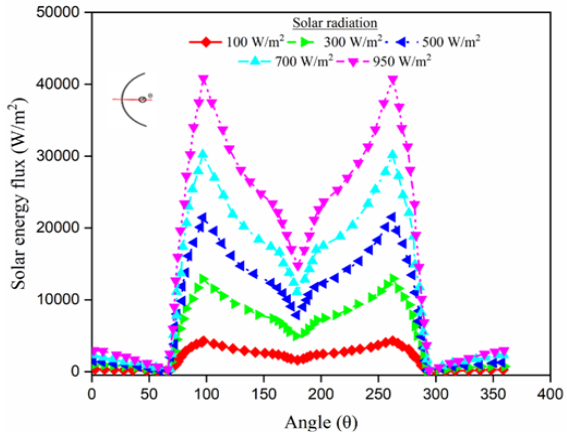

Fig. 6: Validation of solar energy flux distribution over the receiver tube circumference with 937.9 W/m² (Z. D. Cheng et al. (2010)

(a)

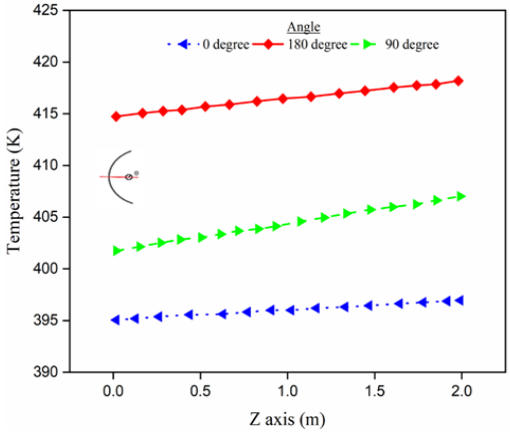

(b)

Fig. 7: Circumferential solar flux distribution on the outer wall of receiver tube of parabolic trough collector for different solar radiations, and (b) Temperature on the receiver tube of parabolic trough collector in an axial direction

3.2 Impact of solar radiation on the efficiency of PTC

Figure 8 (a) shows solar radiation's impact on PTC's efficiency. As we increase solar radiation, PTC efficiency increases by keeping HTF's mass flow rate and inlet temperature constant. (i.e.,1 m/s and 303 K) as presented in Figure 8 (a). Due to increased solar radiation, concentrated solar energy flux on the receiver tube surface also increases. Solar flux on the receiver tube surface is proportional to the solar radiation. Moreover, as the amount of solar radiation rises, the outlet temperature of HTF (Syltherm-800) also rises. The PTC's output and outlet temperature increase by inserting the glass envelope outside the receiver tube, as shown in Figure 8 (a). Efficiency increases by 0.06% by maintaining the constant flow rate and inlet temperature of HTF (i.e., 1 m/s and 303 K). The explanation is that the glass envelope reduces atmospheric convective heat losses.

Figure 8 (b) represents the relationship between the Reynolds number and Nusselt number for the varying solar radiations. Reynolds number remained unchanged as the mass flow rate and inlet flow temperature were kept constant (i.e., 1 m/s and 303 K) while studying the effect of solar radiation on the efficiency of PTC. Nusselt number varies because of the convective heat transfer coefficient change, which keeps changing with the change or increase in solar radiation. An increase in the Nusselt number increases the efficiency of the PTC, as shown in Figure 8 (a).

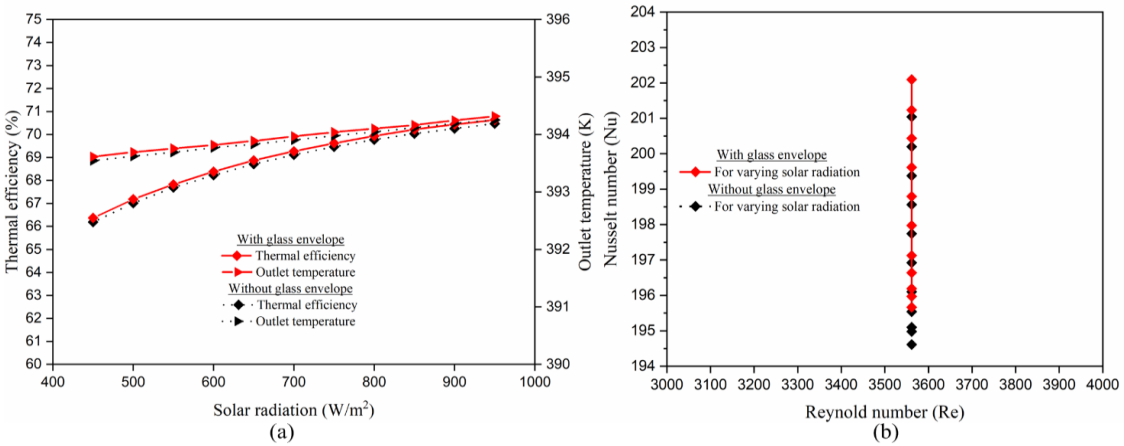

Fig. 8: (a) Efficiency of parabolic trough collector with the variation of solar radiation, and (b) Variation of Reynold number and Nusselt number with the variation of solar radiation

3.3 Impact of mass flow rate on the efficiency of PTC

Figure 9 (a) shows the impact of the mass flow rate of HTF on the PTC's efficiency. As we increase the HTF's mass flow rate, there is an increase in efficiency, but the outlet temperature of the PTC decreases. This is because of the effect of mass flow rate. A higher flow rate combined with a lower temperature difference (i.e., the temperature difference between the inlet and outlet of the absorber tube) increases PTC efficiency. And for the lower flow rate, the higher temperature difference (i.e., the temperature difference between the inlet and outlet of the absorber tube) combined with the lower flow rate reduces the overall efficiency of the PTC by keeping the solar radiation and inlet temperature of the HTF constant (i.e., 950 W/m2 and 303K). Also, for the lower mass flow rate, the higher will be the outlet temperature and the outlet temperature start reducing as we start increasing the mass flow rate of HTF because of less time for the HTF to get heated in the receiver tube of PTC. The glass envelope's addition to the absorber tube increases the efficiency and outlet temperature by 8.5% by keeping solar radiation and inlet HTF temperature constant (i.e., 950 W/m2 and 303K). This is due to less convective heat losses to the atmosphere, as depicted in Figure 9 (a). Figure 9 (b) shows the relation between the Reynolds number and the Nusselt number for varying the mass flow rate of heat transfer fluid. As the velocity of the heat transfer fluid keeps on increasing, the Reynolds number keeps on increasing. As the Reynolds number increases, the convective heat transfer coefficient also increases. This increase in the convective heat transfer coefficient increases the Nusselt number. An increase in the Nusselt number increases the efficiency of the PTC, as shown in Figure 9 (a).

3.4 Impact of HTF's temperature on the efficiency of PTC

Figure 10 (a) shows the collector's efficiency effect of HTF temperature. PTC efficiency increases rapidly for lower HTF temperature due to the higher heat transfer rate due to the higher temperature difference (i.e., the

HTF temperature difference between the inlet and outlet of the absorber tube). Whereas, if we keep raising the HTF temperature, there is no significant increase in the PTC's efficiency as we keep the mass flow rate of HTF and solar radiation constant (i.e., 950 W/m^2 and 1 m/s). The increase in HTF temperature is higher for lower inlet HTF temperature, but the heat transfer rate reduces as we raise the inlet HTF temperature. PTC's total performance and outlet temperature improved by 0.13% as we placed the glass envelope outside the receiver tube, keeping solar radiation and mass flow rate constant (i.e., 950 W/m^2 and 1 m/s). This is due to reduced atmospheric convective heat losses. Figure 10 (b) represents the relations between the Reynolds number and Nusselt number for varying inlet temperatures of heat transfer fluid. As the heat transfer fluid temperature increases, the various properties of the heat transfer fluid changes (such as density, thermal conductivity, specific heat, and viscosity). Change in the properties of the fluid increases the Reynolds number. The Nusselt number changes initially because of the high convective heat transfer coefficient, but later, the change in the convective heat transfer coefficient is not significant enough to increase the Nusselt number. Thus the efficiency of the PTC increases initially, but after that efficiency of the PTC becomes constant with an increase in the fluid inlet temperature (Figure 10 (a)).

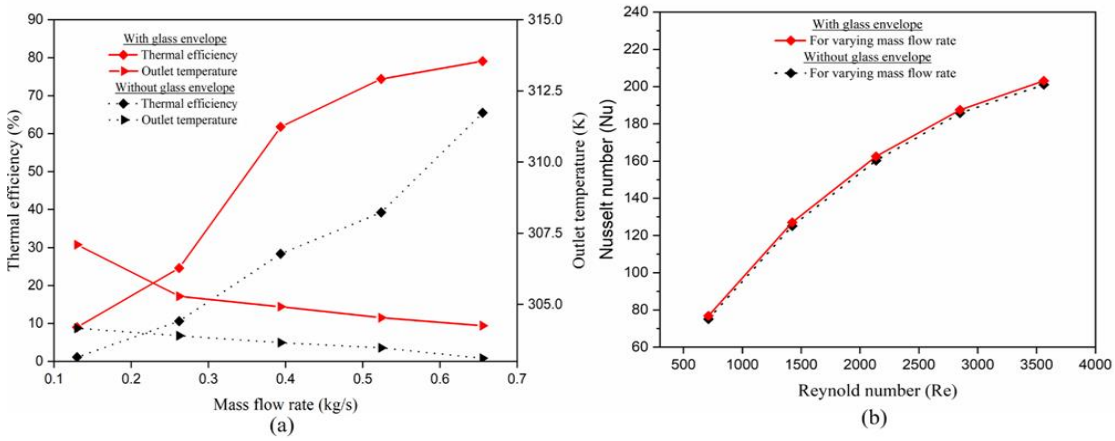

Fig. 9: (a) Efficiency of parabolic trough collector with the variation of heat transfer fluid's mass flow rate, and (b) Variation of Reynold number and Nusselt number with heat transfer fluid's mass flow rate

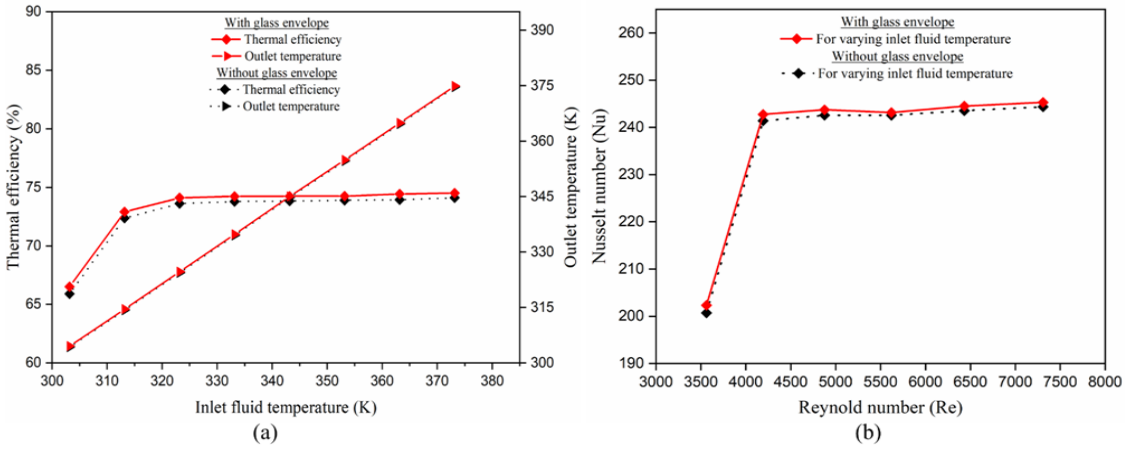

Fig. 10: (a) Efficiency of parabolic trough collector with a variation of inlet heat transfer fluid temperature, and (b) Variation of Reynold number and Nusselt number with inlet heat transfer fluid temperature

3.5 Impact of wind speed on the efficiency of PTC

Figure 12 (a) shows wind speed's effect on parabolic trough collector efficiency. PTC's performance tends to decrease with increased wind speed. It is due to increased ambient heat loss, as shown in Figure 12 (b). The convective heat loss is reduced with the glass envelope used on the absorber tube, as shown in Figure 12 (a). Figure 12 (c) represents the effect of wind speed on the Nusselt number and Reynold number. As the wind speed increases, the Nusselt number keeps on reducing because of higher convective heat loss. This reducing Nusselt number reduces the overall efficiency of the PTC. With the incorporation of glass tubes, the convective heat loss reduces, increasing the overall efficiency compared to the operation of PTC without glass tube.

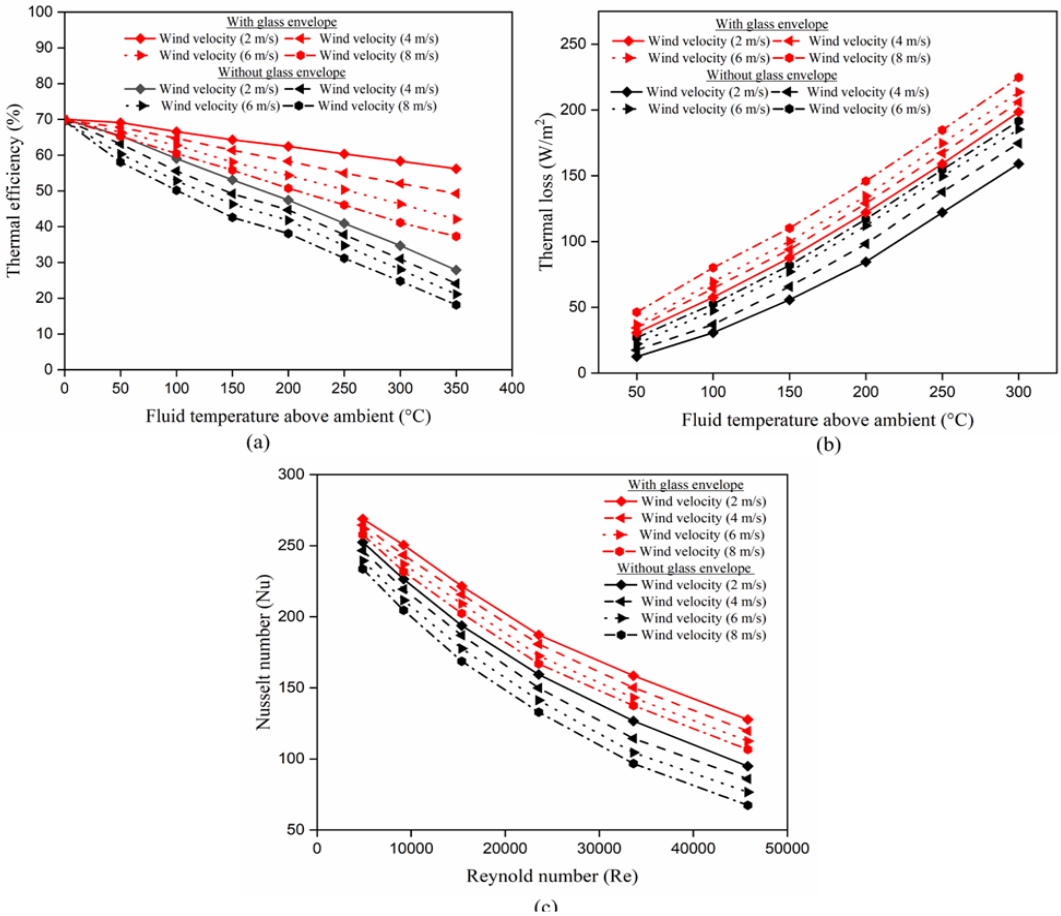

Fig. 12: (a) Effect of wind speed on the efficiency of parabolic trough collector with and without glass envelope, (b) Heat loss from the parabolic trough collector for different wind speeds, and (c) Variation of Reynold number and Nusselt number with different wind speed

4. Conclusions

This paper addressed PTC computational studies using a simple and straightforward approach based on the MCRT method. This algorithm's findings were compared with empirical and experimental research published in the literature as well as with local validation. The maximum relative difference between the new and experimental results was less than 2%. After validation with experiments, two cases were simulated using the same algorithm, i.e., with and without glass envelope, for different real-world parameters (i.e., solar radiation, HTF temperature, mass flow rate of HTF, and wind speed). The findings showed an improvement in efficiency and outlet fluid temperature with an increase in solar radiation. The efficiency and outlet temperature improved further with the addition of a glass envelope outside the receiver tube, as this envelope reduces convective losses to the atmosphere. Furthermore, the efficiency is increased by changing the mass flow rate as convective losses decrease. But the increasing mass flow rate reduces outlet temperature. There is a rapid increase in PTC efficiency for lower inlet fluid temperature, but an increase in efficiency becomes insignificant after specific inlet fluid temperature as the heat transfer rate reduces with the increasing temperature of HTF. Efficiency and outlet temperature increase by using the glass envelope. Wind speed significantly affects PTC's efficiency. PTC efficiency tends to decrease as wind velocity increases due to high convective heat loss. There, too, positioning the glass envelope on the receiver tube increases efficiency.

5. Acknowledgment

The authors gratefully acknowledge the LUIT Renewables and Himachal Pradesh State Council for Science, Technology, and Environment (SCSTE) for providing the experimental data and funding support under the aegis of "Design and development of efficient solar dryer for corrugated box drying" for conducting this research.

6. References

A. Inc., 2018. ANSYS Fluent Theory Guide v18.1," ANSYS 18.1 Doc., vol. 15317, no. April, p. 850.

Almanza, R., Jiménez, G., Lentz, A., Valdés, A., and Soria, A., 2002. DSG under two-phase and stratified flow in a steel receiver of a parabolic trough collector. J. Sol. Energy Eng. Trans. ASME, vol. 124, no. 2, pp. 140–144. https://doi.org/10.1115/1.1463734

Bellos, E., Tzivanidis, C., Said, Z., 2020. A systemetic parametric thermal analysis of nanofluid-based parabolic trough solar collectors. Sustainable Energy Technologies and Assessments, vol. 39. https://doi.org/10.1016/j.seta.2020.100714

Burkhard, D. G., Shealy, D. L., and Sexl, R. U., 1973. Specular reflection of heat radiation from an arbitrary reflector surface to an arbitrary receiver surface. Int. J. Heat Mass Transf., vol. 16, no. 2, pp. 271–280. https://doi.org/10.1016/0017-9310(73)90056-2

Chargui, R., Tashtoush, B., Awani, S., 2021. Experimental study and performance testing of a novel parabolic trough collector. International Journal of Energy Research. https://doi.org/10.1002/er.7267

Cheng, Z. D., He, Y. L., and Cui, F. Q., 2013. A new modelling method and unified code with MCRT for concentrating solar collectors and its applications. Appl. Energy, vol. 101, pp. 686–698. https://doi.org/10.1016/j.apenergy.2012.07.048

Cheng, Z. D., He, Y. L., and Qiu, Y., 2015. A detailed non-uniform thermal model of a parabolic trough solar receiver with two halves and two inactive ends. Renew. Energy, vol. 74, pp. 139–147. https://doi.org/10.1016/j.renene.2014.07.060

Cheng, Z. D., He, Y. L., Wang, K., Du, B. C., and Cui, F. Q., 2014. A detailed parameter study on the comprehensive characteristics and performance of a parabolic trough solar collector system. Appl. Therm. Eng., vol. 63, no. 1, pp. 278–289. https://doi.org/10.1016/j.applthermaleng.2013.11.011

Cheng, Z. D., He, Y. L., Xiao, J., Tao, Y. B., and Xu, R. J., 2010. Three-dimensional numerical study of heat transfer characteristics in the receiver tube of parabolic trough solar collector. Int. Commun. Heat and Mass Transf., vol. 37, no. 7, pp. 782–787. https://doi.org/10.1016/j.icheatmasstransfer.2010.05.002

Dudley, V., Kolb, G., Sloan, M., Kearney, D., 1994. SEGS LS2 solar collector — test results, Report of Sandia National Laboratories, SANDIA94-1884, USA. https://doi.org/10.2172/70756

Evans, D. L., 1977. On the performance of cylindrical parabolic solar concentrators with flat absorbers. Sol. Energy, vol. 19, no. 4, pp. 379–385. https://doi.org/10.1016/0038-092X(77)90009-3

Fan, M., Liang, H., You, S., Zhang, H., Yin, B., and Wu, X., 2017. Performance analysis of a solar heating system with the absorption heat pump and oil/water heat exchanger. Energy Procedia, vol. 142, pp. 97–104. https://doi.org/10.1016/j.egypro.2017.12.016

Hang, Q., Jun, Z., Xiao, Y., and Junkui, C., 2008. Prospect of concentrating solar power in China-the sustainable future. Renew. Sustain. Energy Rev., vol. 12, no. 9, pp. 2505–2514. https://doi.org/10.1016/j.rser.2007.06.002

He, Y. L., Xiao, J., Cheng, Z. D., and Tao, Y. B., 2011. A MCRT and FVM coupled simulation method for energy conversion process in parabolic trough solar collector. Renew. Energy, vol. 36, no. 3, pp. 976–985.

Incropera, F., DeWitt, D., 1990. Fundamentals of Heat and Mass Transfer, John Wiley and Sons, Third Edition, New York, NY.

Jeter, S. M., 1986. Calculation of the concentrated flux density distribution in parabolic trough collectors by a semi-finite formulation. Sol. Energy, vol. 37, no. 5, pp. 335–345.

Kalogirou, S. A., 2012. A detailed thermal model of a parabolic trough collector receiver. Energy, vol. 48, no. 1, pp. 298–306. https://doi.org/10.1016/j.energy.2012.06.023

Mechanics, A. and Arbor, A., 1982. An Analysis of the Technical Performance of a Parabolic for Solar Industrial and Economic Trough. Mech. Eng., vol. 25, no. 9, pp. 1427–1438.

Powar, S., Saini, P., Pandey, S., Dhar, A., 2020. System for cooking eatables. Indian Patents and Trademark Office. 202021049173.

Saini P., Patil D.V., Powar S., 2018. Review on Integration of Solar Air Heaters with Thermal Energy Storage. In: Tyagi H., Agarwal A., Chakraborty P., Powar S. (eds) Applications of Solar Energy. Energy, Environment, and Sustainability. Springer, Singapore. https://doi.org/10.1007/978-981-10-7206-2_9

Saini, P., Powar, S., Dhar A., 2020. System for drying articles. Indian Patents and Trademark Office. 201821038197.

Sokhansefat, T., Kasaeian, A. B., and Kowsary, F., 2014. Heat transfer enhancement in parabolic trough collector tube using Al2O3/synthetic oil nanofluid. Renew. Sustain. Energy Rev., vol. 33, pp. 636–644.

Tzivanidis, C., Bellos, E., Korres, D., Antonopoulos, K. A., and Mitsopoulos, G., 2015. Thermal and optical efficiency investigation of a parabolic trough collector. Case Study. Therm. Eng., vol. 6, pp. 226–237.

Vouros, A., Mathioulakis, E., Papanicolaou, E., Belessiotis, V., 2020. Modelling the overall efficiency of parabolic trough collectors. Sustainable Energy Technologies and Assessments, vol. 40.

Wang, K., Zhang, Z.D., Li, M. J., Min, C. H., 2021. A coupled optical-thermal-fluid- mechanical analysis of parabolic trough solar receivers using supercritical CO_2 as heat transfer fluid. Applied Thermal Engineering, vol. 183, 116154. https://doi.org/10.1016/j.applthermaleng.2020.116154

Zadeh, P. M., Sokhansefat, T., Kasaeian, A. B., Kowsary, F., and Akbarzadeh, A., 2015. Hybrid optimization algorithm for thermal analysis in a solar parabolic trough collector based on nanofluid. Energy, vol. 82, pp. 857–864. https://doi.org/10.1016/j.energy.2015.01.096